



Environmental  
Science  
Nano

**Multi method approach for analysis of road dust particles:  
elemental ratios, SP-ICP-TOF-MS, and TEM**

Journal:	<i>Environmental Science: Nano</i>
Manuscript ID	EN-ART-04-2022-000409.R2
Article Type:	Paper

SCHOLARONE™  
Manuscripts

**Environmental significance:**

The identification, discrimination and quantification of anthropogenic and natural metal-containing nanoparticles (NPs) in the environment is essential to understand the occurrence, fate, behavior and environmental risks of these NPs. In the present study, by combining elemental analysis, SP-ICP-TOF-MS analysis and microscopic analysis, hundreds of millions to tens of billions of Ti-, Pb-, Sn-, and W-containing NPs were detected in road dusts in Shanghai, and the concentrations of anthropogenic Ti-, Pb-, Sn-, and W were estimated. These NPs could originate from the non-exhaust emission of vehicles and coal combustion, and enter the atmosphere and water environment by resuspension and runoff, posing potential risk to human health and aquatic organisms.

1  
2  
3 **Multi method approach for analysis of road dust particles: elemental ratios,**  
4 **SP-ICP-TOF-MS, and TEM**  
5  
6  
7  
8  
9

10 Feiyun Tou<sup>1</sup>, Md. Mahmudun Nabi<sup>2</sup>, Jingjing Wang<sup>2</sup>, Mahdi Erfani<sup>3</sup>, Erfan Goharian<sup>3</sup>, Jing Chen<sup>4</sup>, Yi Yang<sup>1\*</sup>, and  
11 Mohammed Baalousha<sup>2\*</sup>  
12  
13

14  
15  
16  
17 <sup>1</sup> *Key Laboratory of Geographic Information Science (Ministry of Education), School of Geographical Sciences,*  
18 *East China Normal University, 500 Dongchuan Road, Shanghai 200241, China*  
19

20  
21 <sup>2</sup> *Center for Environmental Nanoscience and Risk, Department of Environmental Health Sciences, Arnold School of*  
22 *Public Health, University of South Carolina, Columbia, South Carolina, 29201, United State*  
23

24  
25  
26 <sup>3</sup> *Department of Civil and Environmental Engineering, University of South Carolina, SC 29208, USA*  
27

28  
29 <sup>4</sup> *State Key Laboratory of Estuarine and Coastal Research, Yangtze Delta Estuarine Wetland Ecosystem*  
30 *Observation and Research Station, Ministry of Education & Shanghai, East China Normal University, 3663 North*  
31 *Zhongshan Road, Shanghai 200062, China*  
32  
33

34  
35  
36  
37  
38 **\* Corresponding Author**  
39

40 **Yi Yang** - *Key Laboratory of Geographic Information Science (Ministry of Education); School of Geographical*  
41 *Sciences, East China Normal University, 500 Dongchuan Road, Shanghai 200241, China; Phone: +86-21-*  
42 *54341196; Email: yyang@geo.ecnu.edu.cn*  
43  
44

45  
46  
47 **Mohammed Baalousha** - *Center for Environmental Nanoscience and Risk, Department of Environmental Health*  
48 *Sciences, Arnold School of Public Health, University of South Carolina, Columbia, South Carolina, 29201, United*  
49 *State; Phone: +1-803-777-7177; Email: mbaalous@mailbox.sc.edu*  
50  
51  
52  
53  
54  
55  
56  
57  
58  
59  
60

## Abstract

Road dust particles including nanoparticles (NPs), with heterogeneous composition, are a significant carrier of metals/metalloids and can be further transported into atmosphere or surface runoff. However, their elemental composition remains poorly defined. In this study, seven road dust samples were collected from different areas in Shanghai, China and were analyzed for total metal concentrations, particle elemental composition and ratios, morphology, composition, and crystalline phase. Overall, road dust particles were characterized by high concentrations of Fe, Ti, Al, Cr, Cu, Zn, Sn, and Sb, which varied among samples. Four potential sources of metals were identified using PCA analysis including natural, exhaust, non-exhaust emissions, and vehicle electronics. Bulk elemental ratios of Ti/Nb, Ti/Al, Ti/Fe, Pb/Nb, Sn/Nb and W/Nb in road dust samples were higher than the corresponding reference ratios indicating the road dust contaminations with Ti, Pb, Sn, and W. Anthropogenic Ti, Pb, Sn and W were estimated by mass balance calculation and varied between  $0.25-1.48 \times 10^6 \mu\text{g}\cdot\text{kg}^{-1}$ ,  $0.19-1.21 \times 10^5 \mu\text{g}\cdot\text{kg}^{-1}$ ,  $0.98-4.22 \times 10^4 \mu\text{g}\cdot\text{kg}^{-1}$ , and  $0.12-1.01 \times 10^4 \mu\text{g}\cdot\text{kg}^{-1}$ , respectively. The number concentration of NPs was determined by SP-ICP-TOF-MS and were  $0.66-3.3 \times 10^{10} \text{particle}\cdot\text{g}^{-1}$  of Ti-containing NPs,  $0.23-1.51 \times 10^{10} \text{particle}\cdot\text{g}^{-1}$  of Pb-containing NPs,  $0.28-3.10 \times 10^9 \text{particle}\cdot\text{g}^{-1}$  of Sn-containing NPs, and  $1.34-9.38 \times 10^8 \text{particle}\cdot\text{g}^{-1}$  of W-containing NPs, respectively. TEM analysis further confirmed the occurrence of both natural and anthropogenic Ti- and W-containing NPs and the contamination of Pb- and Sn-containing NPs in Shanghai road dusts. These NPs could originate from the non-exhaust emission of vehicles and coal combustion. Overall, this study provides a reliably comprehensive approach for the characterization of road dust particles and new insights into the nature of Ti-, Pb-, Sn-, and W-containing particles in dust samples.

## 1. Introduction

Air pollution is one of the most important and concerned global environmental issues. Recent studies demonstrated that outdoor air pollution, mostly by fine and inhalable particles with an aerodynamic diameter smaller than  $2.5\ \mu\text{m}$  ( $\text{PM}_{2.5}$ ), has been estimated to lead to 4.14 million premature deaths per year worldwide and contributed to 1.42 million deaths in China.<sup>1-3</sup> Moreover, the airborne ultrafine particles, which are smaller than 100 nm, even can penetrate the alveolar area of lung and transfer with the bloodstream to other organs, including heart and brain.<sup>4-6</sup> With the rapid development of urbanization, an increasing number of natural surfaces (soils, rocks, vegetation, natural surface water) have dramatically shifted to impervious surfaces (buildings, roads, parking lots, sidewalks, *etc.*).<sup>7</sup> Road dust consist of solid particles that are generated by any mechanical processing of materials, including crushing, grinding, rapid impact, handling, detonation, and decrepitation of organic and inorganic materials such as rock, ore, and metal.<sup>8</sup> It can be resuspended into the air as a contributor of  $\text{PM}_{2.5}$  and transported to nearby surface water by urban runoff with significant quantities of contaminants (such as toxic metals and organic pollutants), increasing threats to environmental and human health.<sup>9,10</sup>

It is a great challenge to directly quantify metal-containing particles in complex environmental samples and further differentiate natural from anthropogenic particles. Electron microscopy (EM) techniques, such as scanning transmission electron microscopy (STEM) and scanning electron microscopy (SEM), coupled with accessory capabilities such as energy dispersive X-ray spectrometer (EDS) and selected area electron diffraction (SAED), have been recognized by the scientific community as powerful tools to provide detailed information including particle size, morphology, chemical composition, and crystal structure on a single-particle basis.<sup>7, 11, 12</sup> Although EM techniques can differentiate naturally occurring from anthropogenic particles in some cases,<sup>7,11</sup> they cannot provide quantitative abundance or concentration information. Single particle inductively coupled plasma time-of-flight mass spectrometry (SP-ICP-TOF-MS) is a unique and promising approach that enables multi-element detection and quantification of various metal and metal-containing particles, providing multidimensional information including multi-element composition, size/mass distribution, and number concentration, and it is the only ICP-MS-based method that allows for quantitative untargeted multi-element measurements from individual particles and could enable differentiating natural from anthropogenic particles.<sup>13-16</sup> At present, it has been used to identify and quantify the engineered and natural nanoparticles in soils,<sup>13, 17, 18</sup> surface/rain waters,<sup>14, 18-20</sup> and effluents from a waste water treatment plants<sup>15</sup>.

Shanghai, with an area of 6340 km<sup>2</sup> and a population of more than 24 million, is a sprawling megacity in China. With increasing population, motorization, urbanization and industrial activities, Shanghai is under

1  
2  
3 serious stress from airborne contaminants, including airborne particles. In the present study, seven road  
4 dust samples were collected from different areas in Shanghai, and were characterized with a series of  
5 techniques, including inductively coupled plasma-mass spectrometry (ICP-MS), SP-ICP-TOF-MS, SEM,  
6 and TEM coupled with EDS and SAED. The overall aim of this study was to characterize road dust using  
7 a multi-method analytical approach in order to better understand the nature of particles in road dust and to  
8 develop approaches to differentiate natural from anthropogenic particles and to quantify their  
9 concentrations. The specific objectives of this study are (1) to realize the source apportionment of metals  
10 in dust samples based on the principal component analysis (PCA), (2) to differentiate the natural particles  
11 from the anthropogenic particles and quantify their concentrations, (3) to determine the elemental  
12 composition of multi-metal bearing particles at the single particle level, and (4) to identify the dominant  
13 metal-containing NPs based on electron microscopy techniques. The information generated in this study  
14 will provide a comprehensive approach for the characterization of road dust particles and give new insights  
15 into the nature of metal-containing particles in Shanghai, China.  
16  
17  
18  
19  
20  
21  
22  
23

## 24 **2. Materials and Methods**

### 25 **2.1. Sample collection and preparation**

26  
27  
28  
29 Seven road dust samples were collected from the road surface in various functional areas in Shanghai. The  
30 distribution and the corresponding detailed information of seven road dust samples, i.e. SJP, JIA, WU,  
31 ZSTP, LT, JHSRS, and ECNU, are shown in Fig. 1 and Table 1, respectively. For each road dust sample,  
32 around 30 g of dust were swept from each side of the pavement, along 100 m, using a plastic brush and  
33 tray, and then mixed thoroughly to obtain a homogeneous sample. All samples were passed through a 48-  
34 mesh sieve to remove large particles, debris and fibers, and then stored in valve bags in the dark at room  
35 temperature.  
36  
37  
38  
39

40  
41 Twenty milligrams of the road dust samples were mixed with 30 mL ultrapure water (UPW,  
42 PURELAB Option-Q, ELGA, Buckinghamshire, UK) in 50 mL acid-washed polypropylene centrifuge  
43 tubes and overhead rotated on a tube rotator (Fisher Scientific, Shanghai, China) at 40 rpm overnight. The  
44 well-dispersed mixture was bath sonicated (Branson 2800, 40kHz, Eppendorf, Hamburg, Germany) for 2 h  
45 to disrupt dust microaggregates and enhance the release dispersion of natural particles.<sup>21</sup> The 1  $\mu\text{m}$  size  
46 fraction was then separated by centrifugation (Eppendorf, 5810 R, Germany) at 775 g for 5 min based on a  
47 particle density of  $2.5 \text{ g}\cdot\text{cm}^{-3}$  and Stokes' law calculation<sup>22</sup> and top 20 ml of the supernatant was transferred  
48 into 50 mL acid-washed polypropylene centrifuge tubes and stored at 4 °C before any further analysis. The  
49 collected fractions were diluted 5000-fold in UPW and sonicated for 15 min in a bath sonicator prior to SP-  
50 ICP-TOF-MS analysis.  
51  
52  
53  
54  
55  
56  
57  
58  
59  
60

## 2.2. Elemental analysis

The road dust samples were digested in a custom-made digestion oven in a metal-free HEPA filtered air clean lab. To avoid possible contamination, the digestion oven has a Teflon-covered hotplate secured in a plastic box equipped with double-HEPA filtered forced air. 0.2 g of dust was weighed (Mettler Toledo) and transferred into a 15-mL Teflon digestion vessel (Savillex). The samples were treated with 1 mL of 30% H<sub>2</sub>O<sub>2</sub> and heated on the hot plate at 70 °C for 2 hours to digest organic matter. H<sub>2</sub>O<sub>2</sub> was evaporated after the completion of the reaction. The dried sample was then digested with 2 mL of distilled HF: HNO<sub>3</sub> mixture (3:1, ACS grade acids) at 110 °C for 48 hours. The liquid was evaporated at the end of digestion. 1 mL distilled concentrated HNO<sub>3</sub> (~70%) was added to the residue and left to dry at 110 °C. This step was repeated twice to ensure break down of any possible insoluble fluoride salts generated in the digestion process. The residue was dissolved in 5 mL of 1% HNO<sub>3</sub> (TraceMetal grade, Fisher Chemical), diluted in ultrapure water (UPW, PURELAB Option-Q, ELGA LabWater). The solution was bath sonicated (Branson, Model 2800, 40 kHz) for 10 min and left in the digestion oven at 50 °C for 2 hours. Then the solution was transferred into a 15 mL polypropylene centrifuge tube (10% ACS grade HNO<sub>3</sub> pre-washed, Fisherbrand). Prior to ICP-MS analysis, the samples were centrifuged at 3,100 g for 5 min to remove any undigested minerals, and the supernatant was diluted 1,000 times with 1% TraceMetal grade HNO<sub>3</sub>.

Elemental concentration of the digested samples was determined using Perkin Elmer NexION 350D inductively coupled plasma-mass spectrometer. Standard tuning procedure was performed before analysis for instrument maintenance. Isotopes measured were <sup>24</sup>Mg, <sup>27</sup>Al, <sup>45</sup>Sc, <sup>49</sup>Ti, <sup>51</sup>V, <sup>53</sup>Cr, <sup>55</sup>Mn, <sup>57</sup>Fe, <sup>59</sup>Co, <sup>60</sup>Ni, <sup>65</sup>Cu, <sup>66</sup>Zn, <sup>69</sup>Ga, <sup>72</sup>Ge, <sup>85</sup>Rb, <sup>88</sup>Sr, <sup>89</sup>Y, <sup>90</sup>Zr, <sup>93</sup>Nb, <sup>98</sup>Mo, <sup>107</sup>Ag, <sup>111</sup>Cd, <sup>118</sup>Sn, <sup>133</sup>Cs, <sup>137</sup>Ba, <sup>139</sup>La, <sup>140</sup>Ce, <sup>141</sup>Pr, <sup>142</sup>Nd, <sup>152</sup>Sm, <sup>153</sup>Eu, <sup>158</sup>Gd, <sup>159</sup>Tb, <sup>164</sup>Dy, <sup>165</sup>Ho, <sup>166</sup>Er, <sup>169</sup>Tm, <sup>174</sup>Yb, <sup>175</sup>Lu, <sup>180</sup>Hf, <sup>181</sup>Ta, <sup>184</sup>W, and <sup>195</sup>Pt, <sup>208</sup>Pb, <sup>232</sup>Th, and <sup>238</sup>U. Dissolved multi-element standards mixture of ICP Complete Group Calibration Standard (BDH Chemicals) and ICP Refractory Element Group Calibration Standard (BDH Chemicals) diluted in 1% (v/v) nitric acid (TraceMetal grade, Fisher Chemical) were used for mass concentration calibration ranging from 0.1 to 1000 µg/L. <sup>115</sup>In was monitored as the internal standard (ICP Internal Element Group Calibration Standard, BDH Chemicals) for quality control. Kinetic energy discrimination (KED) Mode (with helium gas flow rates of 0.3-0.45 mL/min) was used to eliminate the polyatomic interference. The parameters of ICP-MS and SP-ICP-TOF-MS were listed in Table S1.

## 2.3. Single particle analysis

Single particle analysis of the diluted dust particle extracts was performed using an ICP-TOF-MS (TOFWERK, Thun, Switzerland) to determine all isotopes within a single particle simultaneously.<sup>23</sup> All samples and procedural blanks were analyzed in triplicates and data were collected for 10 minutes for each

1  
2  
3 replicate. The replicates were combined for all following data analysis due to the low detection frequency  
4 of some elements. Element specific instrument sensitivities were measured with a multi-element solution  
5 mix prepared from a multi-element solution (0, 1, 2, 5, and 10  $\mu\text{gL}^{-1}$  multi element standard, diluted in 1%  
6  $\text{HNO}_3$ , BDH Chemicals, Radnor, PA, USA). The transport efficiency was calculated using the known size  
7 approach<sup>24</sup> using both Au ENMs with a certified particle size of 60 nm (NIST RM8013 Au, Gaithersburg,  
8 MD, USA) prepared in UPW and Au ionic standard solutions (0, 1, 2, 5, and 10  $\mu\text{gL}^{-1}$ , diluted in 1% HCl,  
9 BDH Chemicals, West Chester, PA, USA). Using a standard tuning solution, the ICP-TOF-MS mass spectra  
10 were calibrated based on  $^{18}\text{H}_2\text{O}^+$ ,  $^{59}\text{Co}^+$ ,  $^{115}\text{In}^+$ ,  $^{140}\text{Ce}^+$ , and  $^{238}\text{U}^+$  target isotopes in TofDaq Viewer  
11 (Version, TOFWERK) prior analysis. Particle/baseline signal separation, particle signals, and particles'  
12 mass were determined from the mass-calibrated ICP-TOF-MS spectra using or in Tofware (Version,  
13 TOFWERK). The particle detection threshold was calculated for each isotope according to Eq. 1.<sup>25</sup>  
14  
15  
16  
17  
18  
19  
20  
21

$$\text{Threshold} = \text{Mean} + (3.29 \sigma + 2.71) \quad (\text{Eq. 1})$$

22  
23  
24 Mean and  $\sigma$  are those of background signal in the analysis window of a 100 data points. The data for  
25 each isotope were treated separately, but the time stamps were kept throughout the data processing for every  
26 isotope, allowing for identification of isotope correlations in a single particle.  
27  
28  
29

#### 30 **2.4. Clustering Analysis of SP-ICP-TOF-MS data**

31  
32 The detected NPs were classified into single and multiple metals nanoparticles (smNPs and mmNPs). The  
33 smNPs were considered as their own clusters because the NP mass and number concentrations are not  
34 sufficient to cluster smNPs. The mmNPs were classified into clusters of NPs of similar elemental  
35 composition using an unsupervised data analysis approach (agglomerative hierarchical clustering) using  
36 MATLAB, to identify clusters/groups of NPs of similar elemental composition and to identify their mean  
37 elemental composition, with the aim to identify anthropogenic NPs in the different dust samples. The  
38 mmNPs were processed through a two-stage (*e.g.*, intra- and inter- sample) hierarchical clustering analysis  
39 following the method described elsewhere.<sup>17, 26</sup> First, intra-sample clustering was performed on all metal  
40 masses in each NP to generate clusters that best account for variance in NP metallic composition in each  
41 sample. Correlation distance, which represents the dissimilarity of NP composition to one another, was  
42 used as the distance metric for clustering. A smaller correlation distance indicates that the elemental  
43 compositions of two particles are very close to each other and *vice versa*. After the correlation distance  
44 between all NPs was calculated, hierarchical clustering was performed using average correlation distance.  
45 This step generated a cluster dendrogram for each sample, which was divided into major clusters using a  
46 distance cutoff. The distance cutoff was determined by visually inspecting the dendrogram and through trial  
47 and error in order to minimize the variance/diversity in NP elemental composition in the major clusters. A  
48  
49  
50  
51  
52  
53  
54  
55  
56  
57  
58  
59  
60



cluster representative was determined for each major cluster as the mean of metal mass in individual NPs within each cluster considering all elements that occurred in at least five percent of NPs within the cluster. For each major cluster, the mass fraction of a given metal in each particle was determined as the mass of that metal divided by the sum of masses of all metals in that NP. Then, the mean cluster composition was determined as the mean of metal mass fraction in all NPs in the cluster. Clusters were labeled by the three elements with the highest mean mass fractions within each cluster. Second, inter-sample clustering was performed on the major cluster representatives identified in the intra-sample clustering to group/cluster the similar NP major clusters identified in the different samples. This step generates a cluster dendrogram for intra-sample cluster representatives, which was divided into major clusters using a distance cutoff as performed for the intra sample clusters. Finally, heat maps were generated by comparing the number of NPs in each major cluster among the different samples. Subsequently, selected elemental ratios were determined on a particle-per-particle basis considering all particles containing the two elements and the elemental ratio distribution was determined. The number concentration (NP g<sup>-1</sup>) of the total, smNPs, mmNPs, and cluster members were determined according to Eq. 2.

$$\text{Number concentration} = \frac{\text{Number of detected NPs} \times \text{dilution factor} \times \text{extraction volume}}{\text{acquisition time} \times \text{liquid flow} \times \text{transport efficiency} \times \text{dust mass}} \quad \text{Eq. 2}$$

## 2.5. Calculation of anthropogenic Ti and W concentrations

The anthropogenic titanium concentration was determined by mass balance calculations based on shifts in elemental concentration ratios of Ti/Nb, Ti/Al, and Ti/Fe in road dust relative to the corresponding elemental ratios in 28 core sediment samples (Table S2 and Table S3) collected in the sampling area for the background level of each element.

$$Ti_{\text{natural}} = Nb_{\text{sample}} \times \left(\frac{Ti}{Nb}\right)_{\text{reference}} \quad (\text{Eq. 3})$$

$$Ti_{\text{anthropogenic}} = Ti_{\text{sample}} - Ti_{\text{natural}} \quad (\text{Eq. 4})$$

Where,  $Ti_{\text{natural}}$  is the natural Ti concentration in the sample,  $Ti_{\text{sample}}$  is the total Ti concentration measured in each dust sample,  $(Ti/Nb)_{\text{reference}}$  is the average Ti/Nb concentration ratio of the local reference samples, which were generally in close agreement with the average crustal values (Table S3).  $Ti_{\text{anthropogenic}}$  is the concentration of anthropogenic Ti. Anthropogenic W, Pb, and Sn concentrations were calculated using Eq 3 and 4 by replacing Ti by W, Pb, and Sn and using W/Nb, Pb/ Nb, and Sn/ Nb ratios, respectively.

## 2.6. Transmission electron microscope

Selected samples (SJP and JHSRS) were characterized using scanning and transmission electron microscopy. Each sample was dispersed in Milli-Q water by ultrasonic and then dropped onto a 300-mesh

1  
2  
3 copper TEM grid with a lacey carbon support film (Electron Microscopy Sciences, USA). A Scanning  
4 Electron Microscope (SEM, Hitachi S4800, Japan) equipped with an energy dispersive X-ray spectrometer  
5 (EDS) system and a Transmission Electron Microscope (TEM, JEOL 2100, Japan) coupled with EDS and  
6 selected area electron diffraction (SAED) were applied to characterize the morphology, composition, and  
7 diffraction patterns of the NPs.  
8  
9  
10

## 11 **2.7. Principle component analysis**

12 The principle component analysis (PCA) using SPSS software following varimax rotation method was  
13 applied for the source apportionment of metals in dust samples. PCA is a statistical method of dimension  
14 reduction. It can realize the change from multiple variables (indicators) to a few comprehensive variables  
15 (indicators) which can reflect most information of the original multiple variables.  
16  
17  
18  
19  
20

## 21 **3. Results and discussion**

### 22 **3.1. Elemental contamination**

23 Total concentrations of Al, Ti, V, Cr, Fe, Co, Ni, Cu, Zn, Sn, Ce, Zr, Pb and W in dust samples are shown  
24 in Fig. S1. Ti, Fe and Al, with the average concentrations of  $4.3 \times 10^6$ ,  $3.5 \times 10^7$ , and  $3.1 \times 10^7 \mu\text{g} \cdot \text{kg}^{-1}$ ,  
25 respectively, are the most abundant metals in Shanghai road dusts, which is 2-4 orders of magnitude higher  
26 than all other metals. Zn followed with an average concentration of  $9.2 \times 10^5 \mu\text{g} \cdot \text{kg}^{-1}$ . W exhibited the  
27 lowest abundance, with an average of  $5.2 \times 10^3 \mu\text{g} \cdot \text{kg}^{-1}$  in all dust samples. Noticeably, JHSRS dust  
28 collected near a high-speed rail train station exhibited the highest concentration of Ti, Al, Sn, W, Ce, Zr,  
29 and Zn and elevated concentration of Pb. Zn concentrations were also found in the dust collected from JIA,  
30 a manufacturing industrial area, (Fig. S1). Dust from SJP, near a large-scale sand mining ship factory,  
31 exhibited the highest concentrations of Fe, Co, Cr, V, Ni, Cu, and Pb compared to all other samples (Fig.  
32 S1). Fe was also elevated in LT and JHSRS dust samples. These elevated metals indicate the possibility of  
33 metal contaminations (including metal-containing particles) in the relevant areas.  
34  
35  
36  
37  
38  
39  
40  
41  
42  
43

44 The principal component analysis (PCA) using SPSS software following varimax rotation method was  
45 applied for the source apportionment of metals in dust samples. As presented in Table S4, four components  
46 were identified. **PC1** had the highest loading of Nd, Tb, Dy, Sm, Al, Gd, Ho, Pr, Tm, Er, Zr, Yb, Hf, Lu,  
47 Eu, Nb, Y, Sc, La, Ta, Th, Ce, Ga, Ti, Ag, U and Mg, explaining 51.2% of the variance. Most of these  
48 metals are common rare earth elements, so the PC1 could be heavily influenced by the soil matrix,  
49 dominantly representing the natural source. **PC2** explained 22.3% of the variance and was related to Ni, V,  
50 Fe, Co, Ge, Cu, Mn, Sr, Cr, Mo, and Pt. These elements are commonly used catalysts in vehicle exhaust  
51 converter,<sup>27-29</sup> indicating that the PC2 could represent a source of vehicle exhaust. **PC3** was linked to Sn,  
52  
53  
54  
55  
56  
57  
58  
59  
60

1  
2  
3 Zn, Cd, In, Pb, Ba and W, explaining 14% of the variance. Lead-tin alloy is an important raw material for  
4 industrial manufacturing, containing automobile manufacturing, and W and Zn are also used in car parts  
5 and tires, respectively.<sup>30-33</sup> These metals could be emitted by the friction of the brake pads and other vehicle  
6 components, indicating that the PC3 could represent the metals from the non-exhaust emission. PC4 was  
7 related to Cs and Rb, explaining 7.4% of the variance. Cs and Rb were important material for making  
8 photocells and vacuum tubes, which could be released from the electronic system of cars. Similar  
9 conclusions could be obtained by the correlation analysis. As shown in Table S5, the metals in each PC  
10 group exhibited strong correlations with each other at 0.01 level, indicating the same or similar source.  
11 Some metals showed strong correlation with metals in other PC groups. For example, W in PC3 also showed  
12 strong correlation with La, Ce, Ga in PC1, indicating another source (natural source) of W. This result is  
13 consistent with the single particle analysis of W-containing particles in Section 3.3. In this section, the  
14 natural source and anthropogenic source of W were demonstrated in Shanghai road dusts. To further  
15 confirm the contamination of other metals (such as Ti, Pb, Sn, and W), elemental ratio analysis was  
16 implemented.  
17  
18  
19  
20  
21  
22  
23  
24  
25

### 26 **3.2. Bulk elemental ratios and anthropogenic elemental concentrations**

27  
28 Natural TiO<sub>2</sub> minerals, such as rutile and ilmenite, have been shown to be the dominant carrier (*e.g.*, > 90-  
29 95% of the whole rock content) for Ti, Nb, Ta, Sb, and W, as well as an important carrier (*e.g.*, 5-45% of  
30 the whole rock content) for V, Cr, Mo, and Sn, such as TiO<sub>2</sub>-bearing metamorphic rocks.<sup>34</sup> The bulk  
31 elemental ratio of Ti/Nb, Ti/Al, and Ti/Fe were higher than the average reference elemental ratios (*e.g.*, 284  
32 ± 17, 0.07 ± 0.013, and 0.133 ± 0.020, respectively, Table S3) for all dust samples except for Ti/Fe in SJP  
33 dust (Fig. S2a-c). These findings suggest that all samples were contaminated with anthropogenic Ti-  
34 containing particles. Although Ti/Nb and Ti/Fe for the LT dust, collected near the exit of highway toll  
35 station were lower than the corresponding mean reference ratios, they were still within the natural  
36 variability range (Fig. S2a-c). The lower Ti/Fe in SJP (near a large-scale sand mining ship factory) dust  
37 than the natural reference ratio could be attributed to natural variability in the dust elemental composition  
38 or to co-contamination of road dust with Fe in this dust sample. The former reason can be ruled out because  
39 the Ti/Fe elemental ratios in Ti- and Fe-bearing particles in SJP dust are typical of natural minerals with an  
40 average elemental ratio of 4.7 ± 20.3 (Fig. S3b). Thus, the lower bulk Ti/Fe elemental ratio in San Jia Port  
41 is due to the co-contamination of SJP dust with Fe-bearing particles. On the other hand, the elemental ratios  
42 of Ti/W were lower than the natural elemental ratios (Fig. S2d), suggesting that these dust samples were  
43 contaminated with W. Given that the dust samples were also contaminated with anthropogenic Ti, the  
44 elemental ratios of W/Nb, Pb/Nb, and Sn/Nb were used to identify W, Pb, and Sn contamination (Fig. S2e-  
45 g), where all dust samples exhibited higher W/Nb, Pb/Nb, and Sn/Nb ratios than the natural reference ratios  
46  
47  
48  
49  
50  
51  
52  
53  
54  
55  
56  
57  
58  
59  
60

( $0.11 \pm 0.01$ ,  $1.46 \pm 0.22$ , and  $0.21 \pm 0.03$ , respectively, Table S3), and the average crustal ratio (0.16, 1.42, and 0.18, respectively, Table S3).

The anthropogenic Ti, W, Pb, and Sn concentration was estimated by mass balance calculations based on Ti/Nb, W/Nb, Pb/Nb, and Sn/Nb elemental ratios respectively according to the equation (3) and (4) (Fig. 2). Anthropogenic estimated Ti, Pb, Sn and W were  $0.25\text{-}1.48 \times 10^6 \mu\text{g}\cdot\text{kg}^{-1}$ ,  $0.19\text{-}1.21 \times 10^5 \mu\text{g}\cdot\text{kg}^{-1}$ ,  $0.98\text{-}4.22 \times 10^4 \mu\text{g}\cdot\text{kg}^{-1}$ , and  $0.12\text{-}1.01 \times 10^4 \mu\text{g}\cdot\text{kg}^{-1}$ , respectively. Anthropogenic Ti contamination in road dust might be attributed to particle release from painted surfaces, photocatalytic surfaces, and white road marking.<sup>35, 36</sup> The JHSRS dust sample collected near a high-speed rail train station displayed the highest anthropogenic W, Pb, and Sn concentrations, which might be attributed to railway coating material and/or vehicle brake pads.<sup>30, 32</sup> We note that the estimated anthropogenic elemental concentrations in this study represent the lower bound of the anthropogenic elemental contamination rather than a precise measure of the anthropogenic fraction concentrations. This is because the estimated anthropogenic concentrations could be underestimated due to the co-contamination of the road dust samples with the reference element (*e.g.*, Nb).

### 3.3. Multi element analysis on single nanoparticle

In addition to the principal component analysis and the bulk elemental ratio analysis, multi-element single particle analysis was performed to further identify metal containing particle contamination in the road dust samples. The number concentration of all NPs, single metal NPs (smNPs), and multi-metal NPs (mmNPs) are presented in Fig. 3. Fe (60 to 88% of all NPs), Al (27 to 37%), Ti (7 to 22%), Mn (8 to 15%), Ba (6 to 12%), and Pb (2 to 9%) were the most abundant particles detected by SP-ICP-TOF-MS. All other detected particles represented < 6% of the total number of detected particles (Fig. 3a). A consistent conclusion was obtained by elemental ratio analysis in Section 3.2. Nanoparticles occurred as either smNPs (Fig. 3b) or mmNPs (Fig. 3c). For each element, smNPs accounted for < 50% the total number of detected element (Fig. S4d). The majority of the detected elements occurred as mmNPs (Fig. S4e). The mmNPs were further classified into clusters of particles with similar elemental compositions (Fig. S5). The intra-sample clustering revealed that dust samples contained various classes/groups of mmNPs including Al, Fe, Ti, Mn, Ba, Sr, Zr, Ce, Y, Th, Cr, Ni, Zn, Cu, Sn, Sb, Pb, and W-rich mmNP (Fig. S5a, Fig. 4). The inter-sample clustering revealed that some mmNPs are conserved across all dust samples and others are present in few dust samples (Fig. S5b, Fig. 4). For instance, AlFeTi, FeAlTi, TiFeMn, CeLaNd, ZrYTh, MnBaPb, CePbMn, SrBaCe, and ThUDy were identified in all dust samples; MnBaPb, SnPbSb, ZnMnSn, and CuSnPb were identified in six dust samples; PbBaSn and YThDy were identified in five dust samples; BaPbSe and SbPbCu were identified in four dust samples; TiAlFe and NiSbCr were identified in three dust

1  
2  
3 samples; and ZnCuSn was identified in only one dust sample (Fig. S5b, Fig. 4). Six clusters of Al, Fe, Ti,  
4 Ce, Zr, and Mn-rich particles accounted for the large majority (> 97%) of mmNPs across all samples (Fig.  
5 4). Other clusters with few numbers of mmNPs include Cr, Sn, Zn, Cu, Ni, Sb, and W-rich mmNP clusters.  
6  
7 The mean elemental composition of the major different mmNP clusters is presented in Fig. 5 and S7. It  
8 illustrates that AlFeTi (Ti/Al =  $0.10 \pm 0.02$ ), FeAlTi (Ti/Fe =  $0.23 \pm 0.06$ ), TiFeMn (Ti/Nb =  $346 \pm 108$ ),  
9 CeLaNd (Ce/La =  $1.95 \pm 0.15$ ), and ZrCeY (Zr/Hf =  $37.4 \pm 8.5$ ) clusters are typical of natural occurring  
10 mmNPs (Fig. S6).<sup>17, 18</sup> Other mmNP clusters were mainly rich in Cr, Ni, Zn, Cu, Pb, Sn, and Sb with low  
11 trace concentrations of other elements (Fig. 5). They are attributed to anthropogenic contamination, most  
12 likely brake wear and/or tire emissions,<sup>30-32</sup> which is consistent with the result of elemental analysis in  
13 Section 3.1. Similar results are also observed in urban runoff.<sup>18, 37, 38</sup> Below, we discuss all particles  
14 containing Cr, Ni, Zn, Pb, Sn, and Sb in more detail.  
15  
16  
17  
18  
19  
20

21 **Pb, Zn, Cr, and Ni-bearing NPs.** Pb-, Zn-, Cr-, and Ni-bearing particles represented 2.1 to 9.3%, 0.8  
22 to 4.6%, 0.9 to 6.1%, and 0.2 to 1.0% of all detected particles. These elements were dominantly (> 72%)  
23 associated with Fe-containing particles. The mass elemental ratio of Pb/Fe, Zn/Fe, Ni/Fe, and Cr/Fe in Fe-  
24 bearing particles are presented in Fig. 6 and illustrate that the majority of these elements occur as a minor  
25 phase in iron-rich particles. Pb/Fe, Zn/Fe, and Ni/Fe each exhibit similar ratios in all dust samples  
26 suggesting that each of these particle types might originated from the same source. These elemental ratios  
27 are most likely typical of naturally occurring particles. The average elemental ratios of Pb/Fe, Zn/Fe, and  
28 Ni/Fe determined at the single particle level in soils natural particles are  $0.014 \pm 0.066$ ,  $0.36 \pm 0.54$ , and  
29  $0.022 \pm 0.033$ .<sup>17, 18</sup> Additionally, some particles displayed Pb/Fe, Zn/Fe, and Ni/Fe > 1.0, which correspond  
30 to the particles identified in the Pb, Zn, and Ni rich clusters (Fig. 5). Cr/Fe exhibit a broader distribution,  
31 as well as a higher fraction with mmNPs with Cr/Fe >1.0, in SJP dust (near a large-scale sand mining ship  
32 factory) compared to all other dusts. The majority of Cr- and Fe-bearing particles in JIA, WU, ZSTP,  
33 JHSRS samples exhibit a Cr/Fe ratio of < 0.1, most likely typical of naturally occurring Cr- and Fe-bearing  
34 particles (natural Cr/Fe determined at the single particle level =  $0.08 \pm 0.15$ ).<sup>17</sup> In contrast SJP, LT, and  
35 ECNU dusts contain Cr- and Fe- with higher elemental ratios and in particular SJP dust contain Cr and Fe  
36 containing particles with Cr/Fe elemental mass ratio up to 3, most likely anthropogenic particles such as  
37  $\text{FeCr}_2\text{O}_4$  (Cr/Fe mass ratio = 1.86). This is consistent with the high concentrations of Cr and Fe in SJP dust  
38 as well as the identification of  $\text{FeCr}_2\text{O}_4$  in SJP dust by TEM analysis. Additionally, SJP dust contained a  
39 high proportion of Cr-dominantly containing particles compared to other dust samples (Fig. 6d).  
40  
41  
42  
43  
44  
45  
46  
47  
48  
49  
50  
51

52 **Sn-bearing NPs.** Sn-bearing particles represented 0.3 to 1.8 % of all detected particles (Fig. S4). Sn-  
53 bearing particles were either smNPs (28-44 %) or mmNPs (56-72 %). Within the mmNPs, Sn occurred as  
54 a major phase in SnPbFe cluster, or as trace element in other clusters, dominantly FeAlSn (65-91 % of all  
55  
56  
57  
58  
59  
60

1  
2  
3 Sn mmNPs) and AlFeSn (0-27 % of Sn mmNPs) clusters (Fig. 7a). Sn also occurred in association with  
4 many other elements such as Cr, Mn, Ni, Cu, Zn, Zr, Sb, Pb, etc. The elemental ratio of Sn/Pb in Sn and  
5 Pb-bearing NPs varied between 0.02 and 500 with most particles (>60 %) exhibiting Sn/Pb < 4.0 (Fig. 6e).  
6 These elemental association suggest the anthropogenic nature of Sn, which is widely used in electroplating  
7 industry, and most likely released from the non-exhaust emission of vehicles as all these elements are used  
8 in brake pad and other vehicle component materials.<sup>18, 30, 31</sup>  
9  
10  
11  
12

13 **W-containing NPs.** Few W-containing NPs, accounting for 0.1-0.6 of all detected NPs, were also  
14 identified in all samples as smNPs (28-63% of all W-bearing NPs) and mmNPs (37-72% of all W-bearing  
15 NPs) (Fig. 3). Within mmNPs, W occurred mostly as a minor element in other metal rich particles such as  
16 Fe, Cr, Ti, and Al (Fig. 7b). The identification of W-containing particles (both as smNP and mmNP) and  
17 the higher bulk W/Al elemental ratios than the natural reference elemental ratios (Fig. S2e) suggest the  
18 anthropogenic nature of W in the dust samples. W occurred in association with many other elements such  
19 as Mn, Ni, Cu, Zn, Zr, Sn, Sb, Pb, etc. These elemental association suggest the anthropogenic nature of W  
20 most likely from brake wear emissions as all these elements are used in brake pad material.<sup>18, 32, 33</sup>  
21  
22  
23  
24  
25  
26

### 27 **3.4. Microscopic analysis**

28  
29 Due to the elevated metals in SJP dust and JHSRS dust samples, these two samples were selected for the  
30 electron microscopic analysis, and numerous Ti-, Fe-, Zn-, Ce-La-, Zr-, Pb-, and Sn-containing NPs were  
31 identified in these two dust samples. W-rich particles were observed by SEM in JHSRS dust. In addition,  
32 Ti-containing NPs were observed more frequently in JHSRS dust (around 83 % of Ti-containing NPs were  
33 identified in JHSRS dust), and Fe-containing NPs were more frequently observed in SJP dust (around 80  
34 % of Fe-containing NPs were identified in SJP dust), which was consistent with the results of total elemental  
35 concentration analysis that Ti and Fe were most abundant in JHSRS dust and SJP dust, respectively. The  
36 following describes specifically what was found/determined directly with electron microscopy.  
37  
38  
39  
40  
41  
42

43 **Titanium oxides.** Titanium oxides, including rutile, anatase and their Magnéli phase ( $\text{Ti}_x\text{O}_{2x-1}$ ), with  
44 different sizes ranging from 60 to 400 nm, are ubiquitous in Shanghai dust samples (Fig. 8a, 8c and Fig.  
45 S7). The observed  $d$ -spacings of 2.01 Å and 2.42 Å in different crystals matched the (1 0 4) lattice plane of  
46 rutile and (1 0 3) lattice plane of anatase, respectively. A typical  $\text{Ti}_x\text{O}_{2x-1}$  in the size range of 200-250 nm  
47 was identified with observed  $d$ -spacing of 3.36 and 3.08, corresponding to the (-1 2 0) and (0 0 4) lattice  
48 plane of  $\text{Ti}_4\text{O}_7$  (Fig. 8a). STEM showed that these titanium oxides were often associated with minor  
49 amounts of Ca, Fe, Si, Al, Na and Zn. Titanium oxides are common engineered particles and widely used  
50 in sunscreens, paints and photocatalysts. Moreover, according to the study by Yang et al.,<sup>11</sup>  $\text{Ti}_x\text{O}_{2x-1}$  is a  
51  
52  
53  
54  
55  
56  
57  
58  
59  
60

1  
2  
3 tracer for tracking solid-state emissions worldwide from industrial coal-burning, suggesting the occurrence  
4 of anthropogenic Ti oxide particles in the road dust samples.  
5  
6

7 **Iron-containing particles.** Various Fe-containing NPs (<100 nm) and ultrafine particles (< 1000 nm),  
8 including ilmenite (FeTiO<sub>3</sub>), hematite (Fe<sub>2</sub>O<sub>3</sub>), magnetite (Fe<sub>3</sub>O<sub>4</sub>), pyrrhotite (Fe<sub>(1-x)</sub>S), fayalite (Fe<sub>2</sub>SiO<sub>4</sub>)  
9 and Fe-Cr oxides (FeCr<sub>2</sub>O<sub>4</sub>) were found in SJP dust, and only magnetite was identified in JHSRS dust. For  
10 example, as shown in Fig. S8a, a polygonal monocrystalline ilmenite particle in the size range of 300-400  
11 nm was identified with observed *d*-spacings of 3.65 Å, corresponding to the (0 1 2) lattice plane of ilmenite.  
12 EDS indicated that Si, Mg and small amounts of Mn were also present. Further, hematite, magnetite and  
13 fayalite particles, with a size range of several nanometers to 400 nm, are ubiquitous in dust samples. For  
14 example, as shown in Fig. S8b, around 300 nm hematite was identified with *d*-spacings of 3.62, 2.27 and  
15 2.14 Å, which agreed with (0 1 2), (0 0 6) and (1 1 3) lattice spacings, respectively, for hematite. 200-300  
16 nm magnetite was also identified with *d*-spacings of 2.15, 1.66 and 1.42 Å (Fig. S8d), matched against the  
17 (1 2 2), (0 4 4) and (1 3 5) lattice planes of magnetite. An example of the aggregation of monocrystalline  
18 and polycrystalline fayalite NPs in the size of several nanometers and 100-200 nm, respectively, was shown  
19 in Fig. S8e with the identifying characteristic *d*-spacings of 4.37, 3.69, 3.51 and 2.46 Å, corresponding to  
20 the (1 1 0), (1 0 1), (1 1 1) and (1 1 2) lattice spacings, respectively, for fayalite. As shown in Fig. S8c, a  
21 pyrrhotite aggregate with a crystal size of 50-400 nm was also identified with *d*-spacings of 5.31 and 2.15  
22 Å, which matches its (2 0 -2) and (1 3 3) lattice planes, respectively. A polycrystalline Fe-Cr oxide in the  
23 primary size of several nanometers was also identified with a characteristic *d*-spacing of 3.45 Å (Fig. S8f),  
24 matched against the (2 0 2) lattice plane of FeCr<sub>2</sub>O<sub>4</sub>. According to the STEM, these Fe-containing NPs were  
25 often associated with minor amounts of Ca, Al, Si, K, Mg, Mn, Cr and Zn. Ilmenite and fayalite are common  
26 natural forms of Fe-containing particles. Besides natural source, magnetic particles (including magnetite  
27 and hematite) in road dusts can also derive from coal fly ash (usually spherical)<sup>39</sup> and vehicle emissions by  
28 abrasion of engine or vehicle body material, which are typically non-spherical<sup>7</sup>. The non-spherical magnetic  
29 particles (Fig. S8b and S8d) could be related to the vehicle emission. Moreover, the elemental and  
30 crystallographic analysis by electron microscopy support the observation obtained by other methods. For  
31 instance, Fig. S8a illustrated ilmenite Ti-Fe-containing particles observed by transmission electron  
32 microscopy in good agreement with the Ti/Fe elemental ratios obtained by SP-ICP-TOF-MS (Fig. S3b).  
33  
34  
35  
36  
37  
38  
39  
40  
41  
42  
43  
44  
45  
46  
47  
48

49 **W-containing particles.** Numerous W-containing particles in the size range of 50-700 nm were found  
50 by SEM in the dust sample from Jinshan high speed rail station (Fig. 8b). According to the EDS, these  
51 particles were frequently associated with minor amounts of Ti and Fe. The abundance of W-containing  
52 particles in dust samples collected near a high-speed rail station supports the total elemental concentration  
53  
54  
55  
56  
57  
58  
59  
60

1  
2  
3 and ratio data, suggesting W contamination in the road dust sample (Fig. S2e). As above mentioned, these  
4 W-containing NPs could be derived from the friction of brake pads and other vehicular components.<sup>32, 33, 40</sup>  
5  
6

7 **Other nanoparticles.** Pb-Sn-, Ce-La-, Zn- and Zr-containing NPs were also commonly found in  
8 Shanghai dust samples (Fig. S9-S12). Ubiquitous Pb<sub>2</sub>Sn<sub>2</sub>O<sub>6</sub> nanoparticles in the size range from several  
9 nanometers to 50 nm were observed by SEM and TEM (Fig. S9). These NPs were identified with the  
10 characteristic *d*-spacings of 5.32, 3.23, 2.98 and 2.63 Å, corresponding to the (2 0 0), (1 1 3), (2 3 0) and (2  
11 2 3) lattice spacings of Pb<sub>2</sub>Sn<sub>2</sub>O<sub>6</sub>, respectively, and found to be associated with trace amount of Fe and Au  
12 by EDS. These elemental associations are consistent with those detected by SP-ICP-TOF-MS (Fig. 5f).  
13 This is also consistent with the molar Sn/Pb elemental ratio calculated at the single particle level, where the  
14 majority of the particles display a Sn/Pb < 4 (Fig. 6e). Ce-La-containing NPs in the size range from several  
15 nanometers to 150 nm were identified with the characteristic *d*-spacings of 4.38, 3.38, 2.99 and 2.24 Å,  
16 corresponding to the (0 1 1), (1 1 0), (2 0 0) and (1 2 0) lattice spacings, respectively, for Stillwellite-(Ce)  
17 (Fig. S10). According to the EDS, minor amounts of Nd, Th and Au were often found associated with these  
18 Ce-La-rich particles. These observations are consistent with the elemental composition of the Ce-rich  
19 particle cluster identified by SP-ICP-TOF-MS (Fig. S6d), which is typical of naturally occurring NPs.<sup>17</sup> Zn-  
20 containing particles, including zincite and smithsonite, were found in both dust samples in the size range  
21 of 50-500 nm (Fig. S11), and identified with the characteristic *d*-spacing 2.52 Å and 2.72 Å, in agreement  
22 with the (1 0 1) lattice spacing of zincite and (1 0 4) lattice spacing of smithsonite, respectively. Zr-  
23 containing particles, including Zr-Sc phosphate and baddeleyite, were found in both dust samples in the  
24 size range of 100-200 nm (Fig. S12), and identified with the characteristic *d*-spacing 4.32 Å and 2.91 Å, in  
25 agreement with the (1 0 1) lattice spacing of pretulite and (1 1 1) lattice spacing of baddeleyite, respectively.  
26 According to the EDS, minor amounts of Y and Fe were often associated with these Zr-rich particles. These  
27 observations are consistent with the elemental composition of the Zr-rich particle cluster identified by SP-  
28 ICP-TOF-MS (Fig. S6e) which is typical of naturally occurring NPs.<sup>17</sup> These naturally occurring particles,  
29 such as Stillwellite-(Ce) and pretulite, and incidental particles, such as Pb-Sn containing particles, were in  
30 good agreement with the results of PCA analysis. For instance, the co-existence of Pb and Sn indicated a  
31 Pb-Sn alloy source which has been widely used in electroplating industry.  
32  
33  
34  
35  
36  
37  
38  
39  
40  
41  
42  
43  
44  
45  
46

#### 47 **4. Conclusions**

48  
49  
50 In the present study, a comprehensive analytical approach was used for the characterization, quantification  
51 and discrimination of natural and anthropogenic metal-containing particles from Shanghai road dust. In  
52 addition to the total elemental concentration and elemental ratio analysis based on the bulk dust samples,  
53 the multi-element single particle analysis in Shanghai road dust was achieved using SP-ICP-TOF-MS, and  
54  
55  
56  
57  
58  
59  
60



1  
2  
3 typical NPs were further identified based on TEM coupled with EDS and SAED techniques. The natural  
4 source of Ti and anthropogenic source of W in dust samples were discriminated by PCA analysis on the  
5 total elemental concentrations. The anthropogenic source of W, Ti, Pb, and Sn were further indicated by  
6 correlation analysis and bulk element ratio analysis. The lower bound of anthropogenic Ti, W, Pb, and Pb  
7 concentrations were estimated to be  $0.25-1.48 \times 10^6 \mu\text{g}\cdot\text{kg}^{-1}$ ,  $0.19-1.21 \times 10^5 \mu\text{g}\cdot\text{kg}^{-1}$ ,  $0.98-4.22 \times 10^4 \mu\text{g}\cdot\text{kg}^{-1}$ ,  
8 and  $0.12-1.01 \times 10^4 \mu\text{g}\cdot\text{kg}^{-1}$ , respectively. The number concentrations of Ti, W, Pb, and Sn-containing  
9 NPs in Shanghai road dusts were determined by SP-ICP-TOF-MS and they varied in the range of  $0.66-3.3$   
10  $\times 10^{10}$  particle $\cdot\text{g}^{-1}$  for Ti-containing NPs,  $0.23-1.51 \times 10^{10}$  particle $\cdot\text{g}^{-1}$  for Pb-containing NPs,  $0.28-3.10 \times$   
11  $10^9$  particle $\cdot\text{g}^{-1}$  for Sn-containing NPs, and  $1.34-9.38 \times 10^8$  particle $\cdot\text{g}^{-1}$  for W-containing NPs. Many clusters,  
12 such as MnBaPb, SnPbSb, ZnMnSn, and CuSnPb, were found rich in Cr, Ni, Zn, Cu, Pb, Sn, Sb, and W,  
13 which could be attributed to anthropogenic contamination. Moreover, numerous Ti-, Pb-, Sn- and W-rich  
14 particles, which could originate from the non-exhaust emission of vehicles, were identified in Shanghai  
15 road dusts by TEM. Besides natural TiO<sub>2</sub> NPs, such as rutile and ilmenite, typical Magnéli phase of TiO<sub>2</sub>  
16 NPs were also found in Shanghai Road dust, which could be a tracer for tracking solid-state emissions  
17 worldwide from industrial coal-burning and be considered as the evidence of anthropogenic contamination  
18 of Ti-containing NPs. The analysis of other metal-containing NPs based on this comprehensive analytical  
19 approach are also consistent. For instance, the co-existence of Pb-Sn and Zr-Y in mmNPs were illustrated  
20 by EDS (Fig. S9 and S13), SP-ICP-TOF-MS (Fig. S5), and PCA analysis. Overall, this study provides a  
21 reliably comprehensive approach for the characterization of road dust particles and give new insights into  
22 the nature of Ti-, Pb-, Sn- and W-bearing particles in dust samples.  
23  
24  
25  
26  
27  
28  
29  
30  
31  
32  
33  
34

## 35 **Conflicts of interest**

36  
37  
38  
39 The authors declare that they have no competing interests.  
40  
41

## 42 **Acknowledgements**

43  
44  
45 This study was supported by the National Natural Science Foundation of China (42125102) and the  
46 United States National Science Foundation (Grants No. 1553909 and 1828055). Additional funding for this  
47 work was provided by the Fundamental Research Funds for the Central Universities and the Open  
48 Foundation of East China Normal University (ECNU).  
49  
50  
51

## 52 **Reference**

1. J. Lelieveld, J. S. Evans, M. Fnais, D. Giannadaki and A. Pozzer, The contribution of outdoor air pollution sources to premature mortality on a global scale, *Nature*, 2015, **525**, 367-+.
2. R. A. Rohde and R. A. Muller, Air Pollution in China: Mapping of Concentrations and Sources, *Plos One*, 2015, **10**, e0135749.
3. HEI, State of Global Air 2020, *Health Effects Institute, Boston, MA*, 2020,
4. B. A. Maher, I. A. M. Ahmed, V. Karloukovski, D. A. MacLaren, P. G. Foulds, D. Allsop, D. M. A. Mann, R. Torres-Jardon and L. Calderon-Garciduenas, Magnetite pollution nanoparticles in the human brain, *P. Natl. Acad. Sci. USA*, 2016, **113**, 10797-10801.
5. M. R. Miller, J. B. Raftis, J. P. Langrish, S. G. McLean, P. Samutrtai, S. P. Connell, S. Wilson, A. T. Vesey, P. H. B. Fokkens, A. J. F. Boere, P. Krystek, C. J. Campbell, P. W. F. Hadoke, K. Donaldson, F. R. Cassee, D. E. Newby, R. Duffin and N. L. Mills, Inhaled Nanoparticles Accumulate at Sites of Vascular Disease, *Acs Nano*, 2017, **11**, 4542-4552.
6. B. A. Maher, Airborne Magnetite- and Iron-Rich Pollution Nanoparticles: Potential Neurotoxicants and Environmental Risk Factors for Neurodegenerative Disease, Including Alzheimer's Disease, *Journal of Alzheimers Disease*, 2019, **71**, 361-375.
7. Y. Yang, M. Vance, F. Tou, A. Tiwari, M. Liu and M. F. Hochella, Jr., Nanoparticles in road dust from impervious urban surfaces: distribution, identification, and environmental implications, *Environmental Science: Nano*, 2016, **3**, 534-544.
8. R. K. Khan and M. A. Strand, Road dust and its effect on human health: a literature review, *Epidemiology and Health*, 2018, **40**, e2018013.
9. S. Chen, X. Zhang, J. Lin, J. Huang, D. Zhao, T. Yuan, K. Huang, Y. Luo, Z. Jia, Z. Zang, Y. a. Qiu and L. Xie, Fugitive Road Dust PM2.5 Emissions and Their Potential Health Impacts, *Environ. Sci. Technol.*, 2019, **53**, 8455-8465.
10. D. Salameh, J. Pey, C. Bozzetti, I. El Haddad, A. Detournay, A. Sylvestre, F. Canonaco, A. Armengaud, D. Piga, D. Robin, A. S. H. Prevot, J. L. Jaffrezo, H. Wortham and N. Marchand, Sources of PM2.5 at an urban-industrial Mediterranean city, Marseille (France): Application of the ME-2 solver to inorganic and organic markers, *Atmospheric Research*, 2018, **214**, 263-274.
11. Y. Yang, B. Chen, J. Hower, M. Schindler, C. Winkler, J. Brandt, R. Di Giulio, J. Ge, M. Liu, Y. Fu, L. Zhang, Y. Chen, S. Priya and M. F. Hochella, Jr., Discovery and ramifications of incidental Magneli phase generation and release from industrial coal-burning, *Nature Communications*, 2017, **8**, 194.
12. F. Tou, Y. Yang, J. Feng, Z. Niu, H. Pan, Y. Qin, X. Guo, X. Meng, M. Liu and M. F. Hochella, Environmental Risk Implications of Metals in Sludges from Waste Water Treatment Plants: The Discovery of Vast Stores of Metal Containing Nanoparticles, *Environ. Sci. Technol.*, 2017, **51**, 4831-4840.
13. A. Praetorius, A. Gundlach-Graham, E. Goldberg, W. Fabienke, J. Navratilova, A. Gondikas, R. Kaegi, D. Günther, T. Hofmann and F. von der Kammer, Single-particle multi-element fingerprinting (spMEF) using inductively-coupled plasma time-of-flight mass spectrometry (ICP-TOFMS) to identify engineered nanoparticles against the elevated natural background in soils, *Environmental Science: Nano*, 2017, **4**, 307-314.
14. A. Gondikas, F. von der Kammer, R. Kaegi, O. Borovinskaya, E. Neubauer, J. Navratilova, A. Praetorius, G. Cornelis and T. Hofmann, Where is the nano? Analytical approaches for the detection and quantification of TiO2 engineered nanoparticles in surface waters, *Environmental Science: Nano*, 2018, **5**, 313-326.
15. K. Mehrabi, D. Gunther and A. Gundlach-Graham, Single-particle ICP-TOFMS with online microdroplet calibration for the simultaneous quantification of diverse nanoparticles in complex matrices, *Environmental Science: Nano*, 2019, **6**, 3349-3358.
16. S. Naasz, S. Weigel, O. Borovinskaya, A. Serva, C. Cascio, A. K. Undas, F. C. Simeone, H. J. P. Marvin and R. J. B. Peters, Multi-element analysis of single nanoparticles by ICP-MS using quadrupole and time-of-flight technologies, *J. Anal. At. Spectrom.*, 2018, **33**, 835-845.

17. M. Baalousha, J. Wang, M. Erfani and E. Goharian, Elemental fingerprints in natural nanomaterials determined using SP-ICP-TOF-MS and clustering analysis, *The Science of the total environment*, 2021, **792**, 148426.
18. J. Wang, M. M. Nabi, M. Erfani, E. Goharian and M. Baalousha, Identification and quantification of anthropogenic nanomaterials in urban rain and runoff using single particle-inductively coupled plasma-time of flight-mass spectrometry, *Environmental Science-Nano*, 2022, **9**, 714-729.
19. M. M. Nabi, J. Wang and M. Baalousha, Episodic surges in titanium dioxide engineered particle concentrations in surface waters following rainfall events, *Chemosphere*, 2021, **263**, 128261.
20. M. M. Nabi, J. Wang, E. Goharian and M. Baalousha, Temporal variation in TiO<sub>2</sub> engineered particle concentrations in the Broad River during dry and wet weathers, *Sci. Total Environ.*, 2022, **807**, 151081.
21. F. Loosli, Z. Yi, D. Berti and M. Baalousha, Toward a better extraction of titanium dioxide engineered nanomaterials from complex environmental matrices, *NanoImpact*, 2018, **11**, 119-127.
22. Z. Tang, L. Wu, Y. Luo and P. Christie, Size fractionation and characterization of nanocolloidal particles in soils, *Environ. Geochem. Health*, 2009, **31**, 1-10.
23. L. Hendriks, A. Gundlach-Graham, B. Hattendorf and D. Guenther, Characterization of a new ICP-TOFMS instrument with continuous and discrete introduction of solutions, *J. Anal. At. Spectrom.*, 2017, **32**, 548-561.
24. H. E. Pace, N. J. Rogers, C. Jarolimek, V. A. Coleman, C. P. Higgins and J. F. Ranville, Determining Transport Efficiency for the Purpose of Counting and Sizing Nanoparticles via Single Particle Inductively Coupled Plasma Mass Spectrometry, *Anal. Chem.*, 2011, **83**, 9361-9369.
25. M. Tanner, Shorter signals for improved signal to noise ratio, the influence of Poisson distribution, *J. Anal. At. Spectrom.*, 2010, **25**, 405-407.
26. K. Mehrabi, R. Kaegi, D. Gunther and A. Gundlach-Graham, Emerging investigator series: automated single-nanoparticle quantification and classification: a holistic study of particles into and out of wastewater treatment plants in Switzerland, *Environmental Science-Nano*, 2021, **8**, 1211-1225.
27. M. M. Maricq, Chemical characterization of particulate emissions from diesel engines: A review, *J. Aerosol Sci*, 2007, **38**, 1079-1118.
28. H. M. Prichard and P. C. Fisher, Identification of Platinum and Palladium Particles Emitted from Vehicles and Dispersed into the Surface Environment, *Environ. Sci. Technol.*, 2012, **46**, 3149-3154.
29. Y. F. Wang, K. L. Huang, C. T. Li, H. H. Mi, J. H. Luo and P. J. Tsai, Emissions of fuel metals content from a diesel vehicle engine, *Atmos. Environ.*, 2003, **37**, 4637-4643.
30. F. P. Kukutschová Jana, Review of Brake Wear Emissions: A Review of Brake Emission Measurement Studies: Identification of Gaps and Future Needs, *Non-Exhaust Emissions*, 2018, 123-146.
31. A. Thorpe and R. M. Harrison, Sources and properties of non-exhaust particulate matter from road traffic: A review, *Sci. Total Environ.*, 2008, **400**, 270-282.
32. C. T. Foo, B. Omar and A. S. Jalil, A review on recent wheel/rail interface friction management, *Journal of Physics: Conference Series*, 2018, **1049**, 012009
33. A. Furberg, R. Arvidsson and S. Molander, Dissipation of tungsten and environmental release of nanoparticles from tire studs: A Swedish case study, *Journal of Cleaner Production*, 2019, **207**, 920-928.
34. T. Zack, A. Kronz, S. F. Foley and T. Rivers, Trace element abundances in rutiles from eclogites and associated garnet mica schists, *Chem. Geol.*, 2002, **184**, 97-122.
35. D. P. Macwan, P. N. Dave and S. Chaturvedi, A review on nano-TiO<sub>2</sub> sol-gel type syntheses and its applications, *Journal of Materials Science*, 2011, **46**, 3669-3686.
36. M. T. Noman, M. A. Ashraf and A. Ali, Synthesis and applications of nano-TiO<sub>2</sub>: a review, *Environmental Science and Pollution Research*, 2019, **26**, 3262-3291.
37. E. R. McKenzie, J. E. Money, P. G. Green and T. M. Young, Metals associated with stormwater-relevant brake and tire samples, *Sci. Total Environ.*, 2009, **407**, 5855-5860.
38. M. Legret and C. Pagotto, Evaluation of pollutant loadings in the runoff waters from a major rural highway, *Sci. Total Environ.*, 1999, **235**, 143-150.

- 1  
2  
3 39. J. Wu, F. Tou, Y. Yang, C. Liu, J. C. Hower, M. Baalousha, G. Wang, M. Liu and M. F. Hochella, Jr.,  
4 Metal-Containing Nanoparticles in Low-Rank Coal-Derived Fly Ash from China: Characterization and  
5 Implications toward Human Lung Toxicity, *Environ. Sci. Technol.*, 2021, **55**, 6644-6654.  
6  
7 40. D. M. Chapman, Behavior of titania-supported vanadia and tungsta SCR catalysts at high temperatures  
8 in reactant streams: Tungsten and vanadium oxide and hydroxide vapor pressure reduction by surficial  
9 stabilization, *Applied Catalysis a-General*, 2011, **392**, 143-150.  
10  
11  
12  
13  
14  
15  
16  
17  
18  
19  
20  
21  
22  
23  
24  
25  
26  
27  
28  
29  
30  
31  
32  
33  
34  
35  
36  
37  
38  
39  
40  
41  
42  
43  
44  
45  
46  
47  
48  
49  
50  
51  
52  
53  
54  
55  
56  
57  
58  
59  
60

Table 1 Description of sampling sites.

	Sampling site	Location/District	Latitude (°N)	Longitude (°E)	Sites ambient environment
1	San Jia port	Pudong	31°22'08"	121°30'12"	near a large-scale sand mining ship factory
2	Jingiao Industrial Area	Pudong	31°14'52"	121°36'23"	in a manufacturing industrial park
3	Wujiaochang	Yangpu	31°18'18"	121°30'37"	in a densely populated and busy cars commercial district
4	Zhangjiang Science and Technology park	Pudong	31°14'45"	121°42'15"	in a high-tech industrial park
5	Luoqing Town	Baoshan	31°28'17"	121°19'25"	heavy traffic density road, near the exit of highway toll station
6	Jinshan high speed rail station	Jinshan	30°43'50"	121°21'57"	near a high-speed rail train station
7	East China Normal University	Minhang	31°2'14"	121°27'36"	in university campus

Note: Samples analyzed by TEM were highlighted in green. These samples were selected due to the high concentrations of suspected particulate contamination in these two sites.

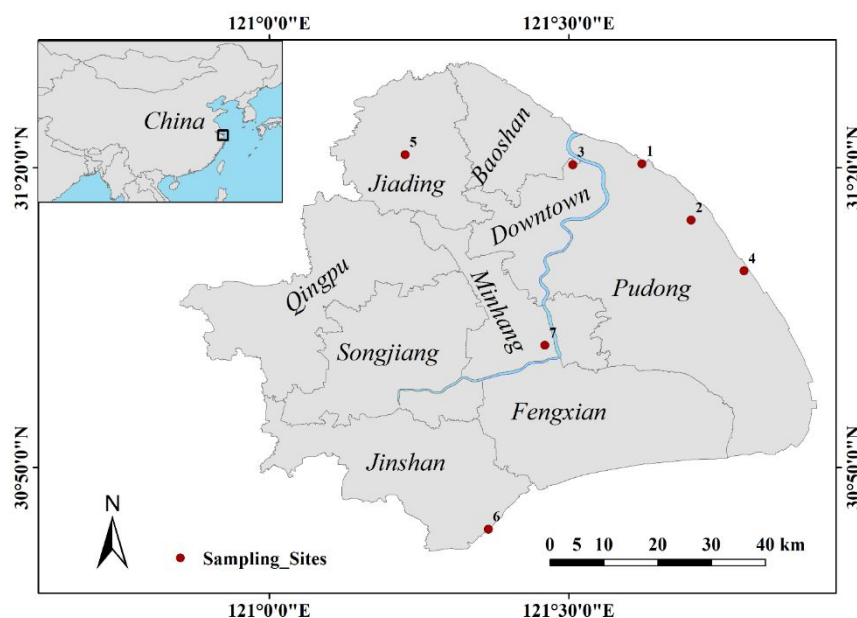
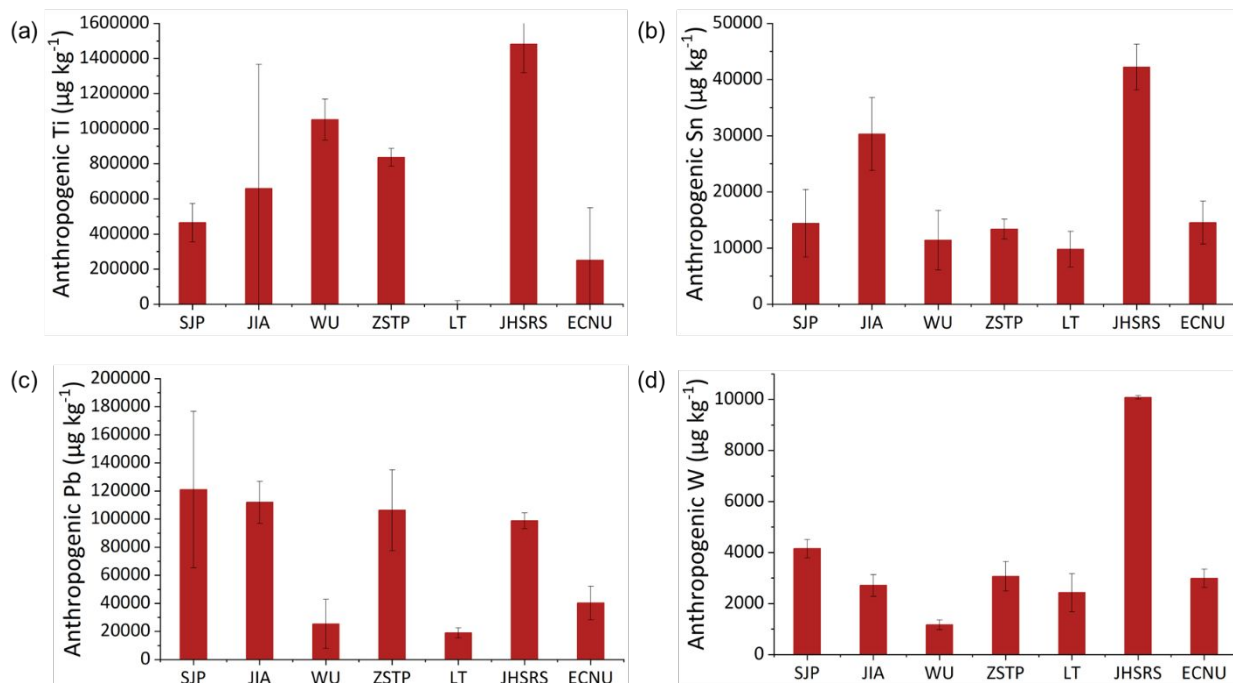
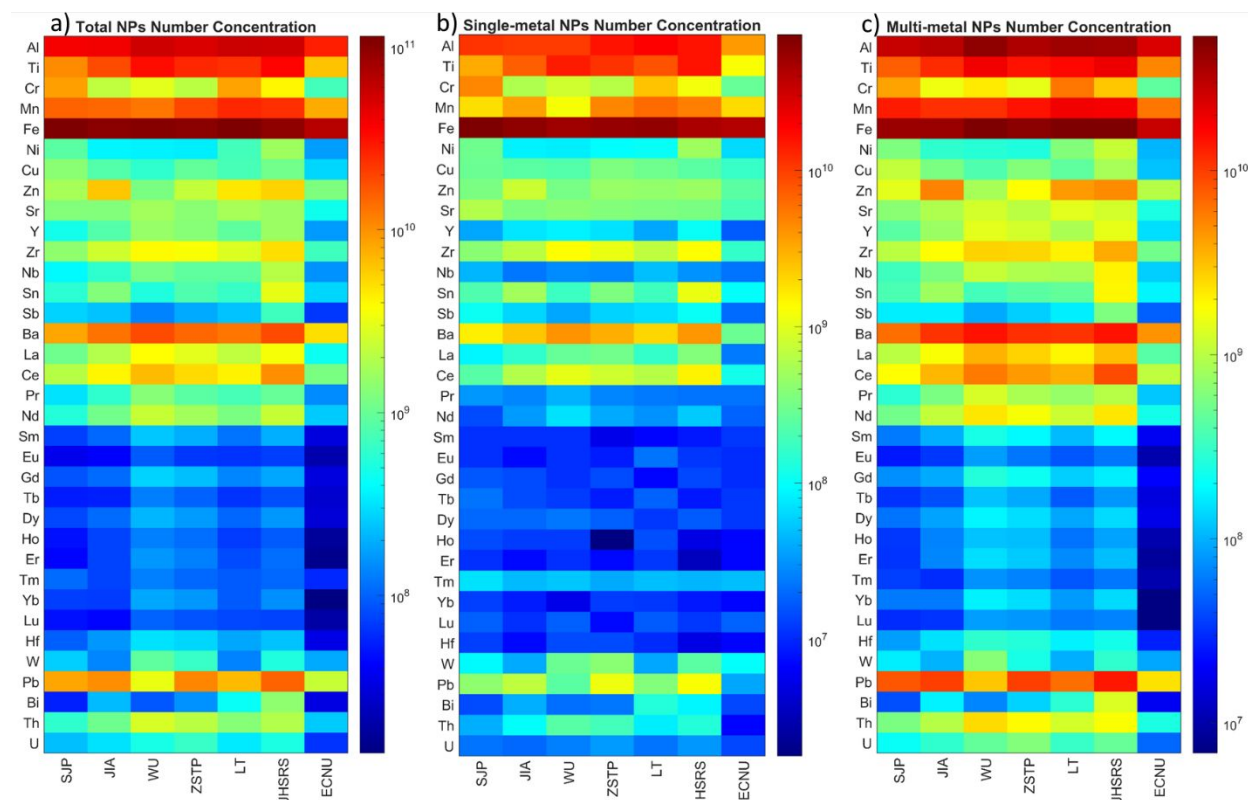


Fig. 1 Distribution of Sampling Sites.



**Fig. 2** Estimated anthropogenic (a) Ti, (b) Sn, (c) Pb, and (d) W concentrations using mass balance calculations and shifts in Ti/Nb, W/ Nb, Pb/ Nb, and Sn/ Nb, respectively.



**Fig. 3** Heat maps of the number concentration (particle/g) of (a) total number of NPs, (b) single metal NPs (smNPs), and (c) multi metal NPs (mmNPs) measured by SP-ICP-TOF-MS.

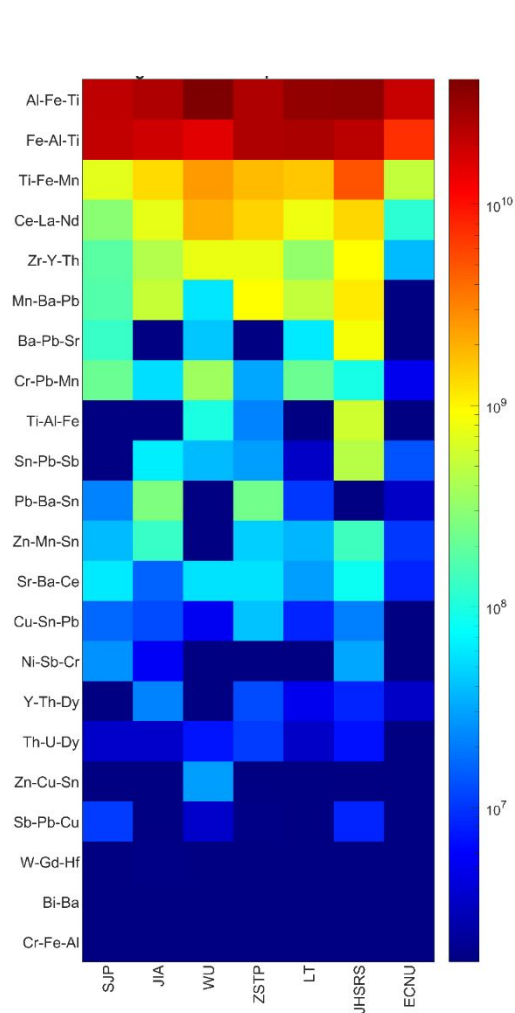


**Fig. 4** Heat maps of the number concentration (particle/g) mmNPs in all dust samples. First and second stage distance cutoffs were set at 0.5 and 0.1, respectively. Clusters are labeled by the three elements with the highest mass fractions in each cluster.

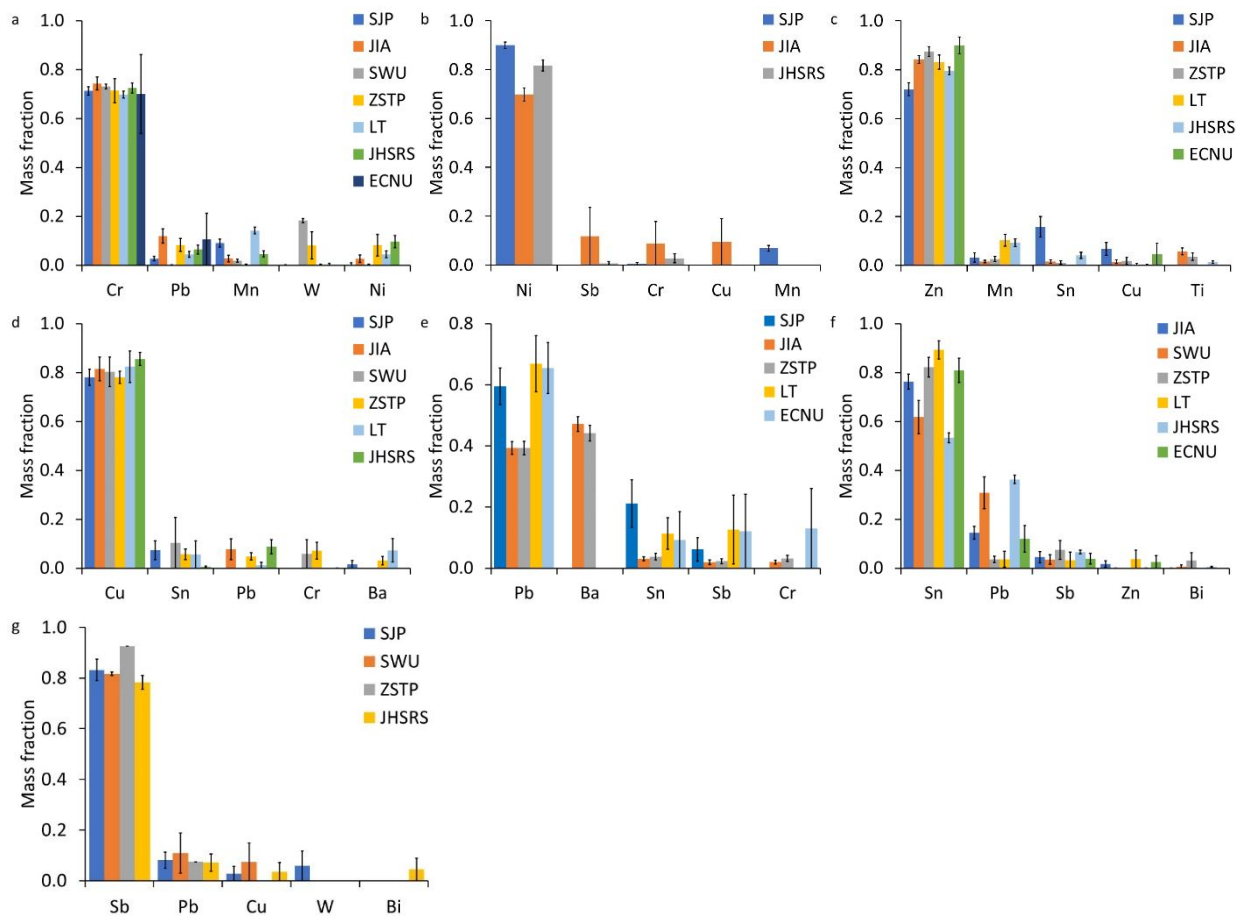


**Fig. 5** Mean elemental mass composition of anthropogenic mmNP clusters identified in the dust samples (a) Cr-, (b) Ni-, (c) Zn-, (d) Cu-, (e) Pb-, (f) Sn-, and (g) Sb-bearing particles.



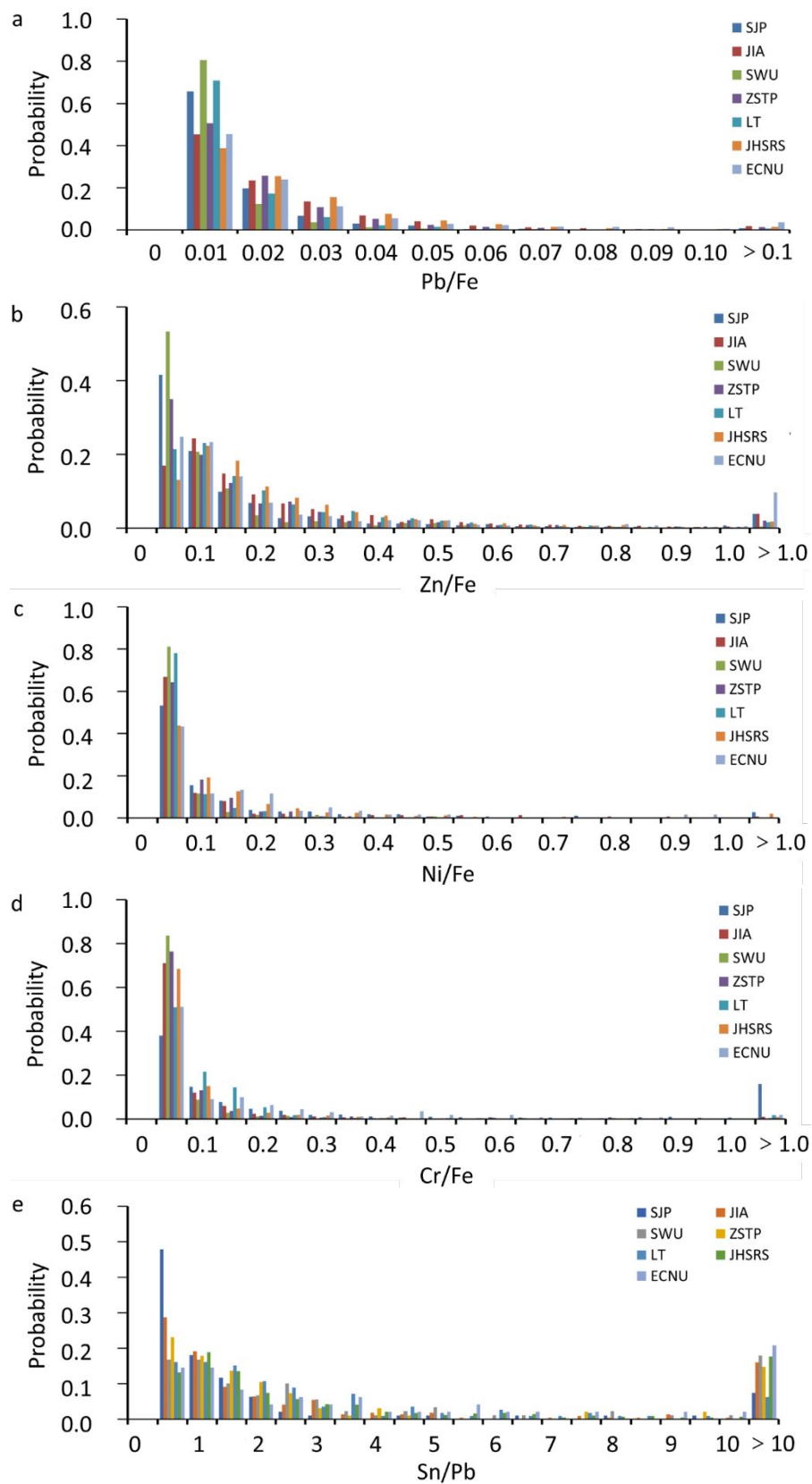


**Fig. 6** Mass elemental ratio of (a) Pb/Fe, (b) Zn/Fe, (c) Ni/Fe, (d) Cr/Fe, and (e) molar elemental ratio of Sn/Pb.

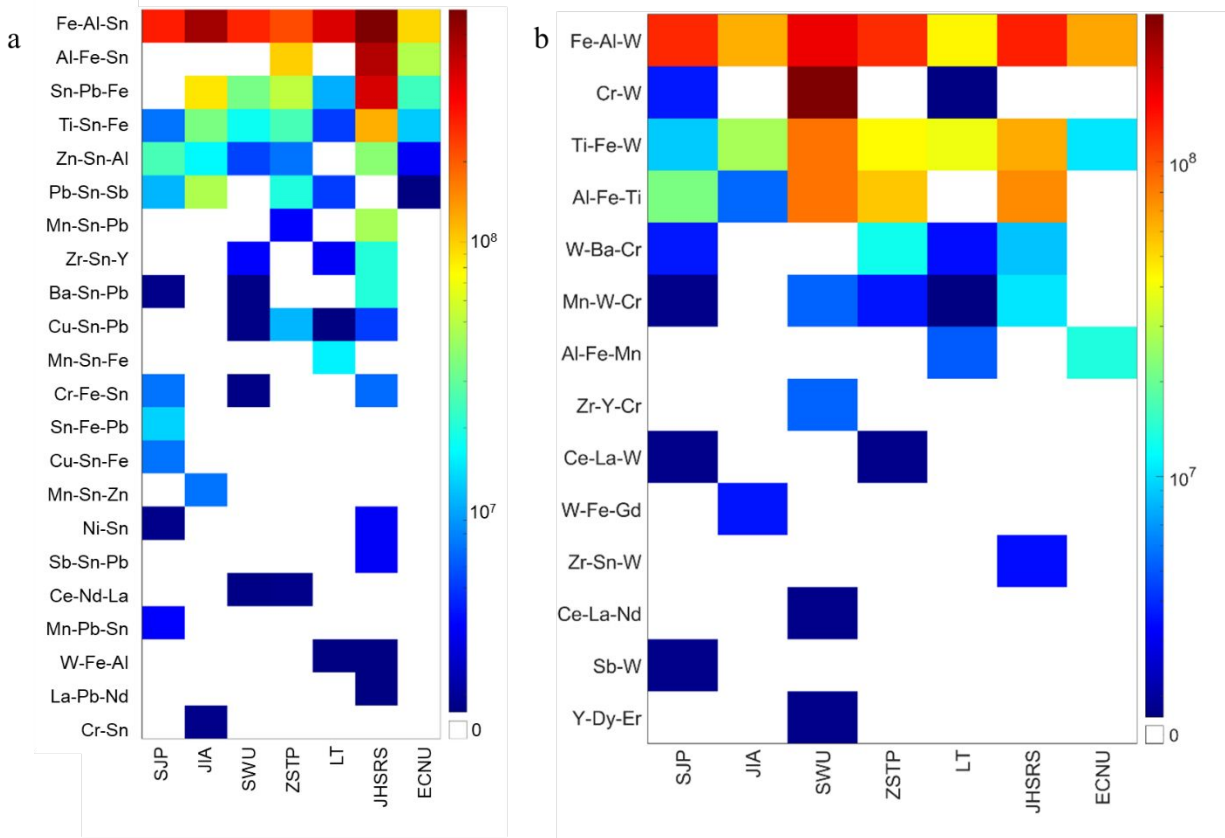
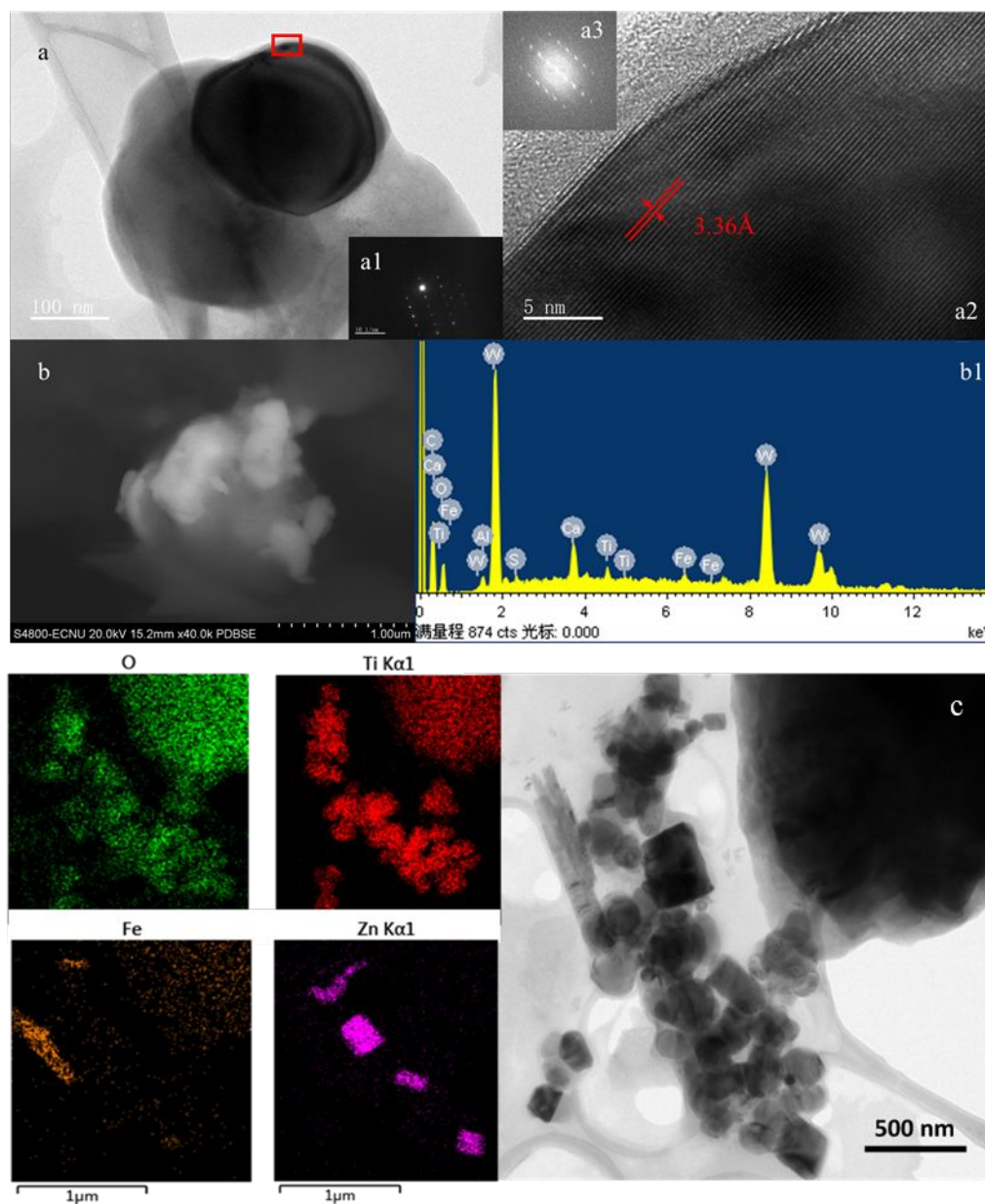


Fig. 7 Reclusing of (a) Sn-bearing mmNPs and (b) W-bearing mmNPs.



**Fig. 8** Typical electron microscopy micrographs of Ti-containing NPs (a:  $\text{Ti}_4\text{O}_7$ ) and W-containing particles (b) in dust samples, among which, a1 and a2 were the corresponding SEAD image and magnification of selected area of a, and a3 was the FFT of a2, and c: STEM images of Ti, Fe, and Zn oxide nanoparticles in dust samples.